IEEE Access
Multidisciplinary ⋮ Rapid Review ⋮ Open Access Journal

Received March 3, 2022, accepted April 18, 2022, date of publication April 22, 2022, date of current version April 29, 2022.

Digital Object Identifier 10.1109/ACCESS.2022.3169510

SAR Image Change Detection Based on Heterogeneous Graph With Multiattributes and Multirelationships

JUN WANG[1,3] AND ANJUN ZHANG[2,3]

[1]School of Mechanical Engineering, Quzhou University, Quzhou, Zhejiang 324000, China
[2]School of Internet, Anhui University, Hefei, Anhui 230000, China
[3]Anhui Province Key Laboratory of Industry Safety and Emergency Technology, Hefei, Anhui 230000, China

Corresponding author: Jun Wang (36110@qzc.edu.cn)

This work was supported in part by the National Natural Science Foundation of China under Grant 62101206 and Grant 62102227, in part by the Key Research and Development Projects of Zhejiang Province under Grant 2020C02SA903678, and in part by the Zhejiang Provincial Natural Science Foundation of China under Grant LZY22D010001.

ABSTRACT The performance of change detection between synthetic aperture radar (SAR) images mainly depends on the selection and utilization of image attributes. Nevertheless, most existing change detection approaches merely take the intensity attribute into consideration, constraining their capacities of detecting changes in complex situations. To solve this problem, this study develops an unsupervised SAR image change detection approach based on heterogeneous graph with multi-attributes and multi-relationships. First, the structural attribute, obtained by removing the complex texture, can be used to reflect the overall features of a SAR image. A heterogeneous graph is then constructed to encode the structural and intensity attributes as vertices, and two types of edges are hence connected to capture the intra-relationships and inter-relationships from these different attributes. With the support of this graph, the hyper-adjacency characteristics are proposed to quantify the multi-relationships and describe the global heterogeneous information. Constructing heterogeneous graphs respectively on bi-temporal SAR images, the changes of both intensity and structural attributes can be measured via comparing the hyper-adjacency characteristics of the bi-temporal graphs, thereby generating a difference image with good separability. Finally, the change map is obtained by cutting off the weakly related edges of heterogeneous graph on the difference image. Experiments on four real SAR datasets prove the effectiveness of the proposed graph-driven approach in improving the accuracy and robustness of change detection.

INDEX TERMS Change detection, synthetic aperture radar, heterogeneous graph, multi-attributes, multi-relationships, hyper-adjacency characteristic.

I. INTRODUCTION

Synthetic aperture radar (SAR) is a significant and stable information source for remote sensing research due to its imaging independence of any sunlight azimuths and atmospheric environment [1]. In recent years, SAR image change detection technology, which identifies changes via analyzing bi-temporal SAR images covering the same geographical region, has caused increasingly more attention [2]. This technology always plays an important role in many earth observation applications, such as environmental assessment [3], urban planning [4], agricultural survey [5] and disaster monitoring [6]. Nevertheless, the inherent speckle noise restricts the development of SAR image change detection.

In general, SAR image change detection technology falls into two main categories, including supervised approaches and unsupervised approaches [7]. Among them, most of these supervised approaches start by classifier training using a mass of labeled data, and then the trained classifier is used to predict the change detection results [8]. The unsupervised approaches can directly measure the change level of candidate images without any prior information. Therefore, scholars are more inclined to adopt the unsupervised approaches rather than supervised ones because of the burdensome data labeling in practical applications [9].

The associate editor coordinating the review of this manuscript and approving it for publication was Gianluigi Ciocca.

For unsupervised patterns, change detection between bi-temporal SAR images generally involves three pivotal steps [10]: (1) images preprocessing, (2) difference image generation and (3) difference image analysis. In the first step, radiometric correction and co-registration technology are applied to align bi-temporal SAR images to the same spectral domain and spatial domain. The second step is to generate a difference image which can reveal various clues about the real changes through comparing the attributes of bi-temporal images. What follows is dividing the difference image into unchanged and changed regions using binary classification approach. In fact, the quality of the change detection relies on the separability of difference image and the accuracy of classification. With the presence of speckle noise, however, satisfactory results for difference image generation and difference image analysis are usually hard to acquire.

Generating a difference image with good separability is an important premise for SAR image precise change detection. The key issue here is how to accurately describe the change levels of SAR images under the negative impact of speckle noise. In this context, compared to subtraction operator, the ratio operator is more suitable for SAR image change detection tasks since the inherent speckle noise obeys the multiplicative model [11]. Moreover, the log-ratio operator, developed by introducing logarithm operation to the ratio operator, can not only convert the multiplicative noise into additive noise, but also compress the range of ratio difference [12]. These pixel-based approaches are decent choices for change detection if the SAR images are not disturbed by the randomness of noise. To further suppress the speckle noise interference during SAR image change detection, the mean-ratio operator, which measures changes through contrasting the means of bi-temporal pixel patches, is also applied [13]. Nevertheless, this approach cannot accurately reflect changes when the compared patches possess the same means but diverse textures. To solve this problem, scholars propose to calculate the local statistics of patches by using probability density functions, and employ the Kullback-Leibler divergence as a distance function for change measure [14]. Inspired by the idea of non-local mean filtering [15], scholars also adopt the similarity of patches to measure changes, and thus generating a smooth difference image [16]. In fact, these patch-based approaches still have room for development in boundary description of changed areas. Therefore, authors propose a neighborhood-based change detection approach, which consists of pixel-based and patch-based operators. Meanwhile, they apply the local variance to adjust the dominance of operators, thereby improving the integrality of changes [17]. Then, the authors employ image fusion strategy to synthesize the complementarity of different operators, acquiring a difference image with highlighted changed regions [18]. The approaches above are certainly effective for speckle suppression, but it is difficult for them to generate difference image with good separability, as only intensity attribute is utilized. Although some scholars have tried to use the textural [19] or structural [20] attribute to improve the presentation of changes, the separability of their difference images remains insufficient because of single attribute utilization. Therefore, there is an urgent need to develop a multi-attribute joint approach for difference image generation.

Difference image analysis is mainly to obtain a change map by dividing the generated difference image into changed and unchanged portions. It is essentially a binary classification problem, so that many promising algorithms in image segmentation field can be transferred to difference image analysis. Among them, automatic thresholding approach is often utilized to rapidly binarize the pixels of difference image [21]. However, thresholding cannot always ensure the accuracy of binary classification, because the statistical model is difficult to exactly describe the intensity distribution of SAR image. Some scholars suggest to take advantage of fuzzy c-means (FCM) clustering to generate the change map [22]. Considering the sensitivity of the standard FCM to speckle noise, scholars introduce the neighbor information into the algorithms to improve the robustness of change detection [23]. These clustering algorithms have the advantage of not requiring to create statistical models, but they are often trapped at locally optimal values due to the application of only a single objective function. Therefore, an artificial immune multi-objective clustering algorithm is proposed to search for the optimal clustering centers of pixels, labeling them as changed or unchanged [24]. Recently, authors employ the FCM clustering to automatically obtain pseudo-labels, and select the samples with higher probabilities to be changed and unchanged for classifier training [25]. Hereafter, the trained deep learning networks are applied to divide the difference image into changed and unchanged classes [26]. These approaches tend to yield superior change maps, since prior information is utilized to train the classifier. However, there are also some limitations, like random sampling would lead to unstable results, and completely reliable prior information is hard to acquire in regions with ambiguous probabilities. At present, spatial context information has received wide attention in SAR image change detection research due to the fact that the changes of pixels are locally correlative. In [27], a modified Markov random field (MRF) model, which combines the nonlocal means similarity weights, is proposed to preserve spatial details and reduce speckle effects in urban change detection. Moreover, researchers apply the multiple kernel graph cuts to extract the changed areas on high-dimensional feature space [28]. For purpose of establishing a broader context relation, the stereo-graph cuts algorithm is constructed between bi-temporal SAR to generate a smooth change map [29]. In summary, utilizing spatial relationships is an effective way to improve the performance of change detection. Nevertheless, approaches above focus on exploring the spatial context relationship of a single attribute, which constrains the sensitivity of detecting object changes in complex scenes. Therefore, the intra-relationships and inter-relationships of different attributes should be taken into consideration when performing change detection tasks.

To solve the problems mentioned above, a novel SAR image change detection approach based on heterogeneous graph with multi-attributes and multi-relationship is proposed. The main contributions are as follows.

(1) A heterogeneous graph is constructed to realize the multi-attributes description about the terrain in a SAR image. In the heterogeneous graph, the intensity and structural attributes are incorporated into vertices, and the multiple relationships of these attributes can be expressed as edges.

(2) A hyper-adjacency matrix is generalized to quantify the intra-relationships and inter-relationships of different attribute vertices, and then the hyper-adjacency characteristic is derived to describe the global heterogeneous information of the graph. The changes of different attributes can be both measured via comparing the hyper-adjacency characteristics of the bi-temporal graphs, thereby generating a difference image with good separability.

(3) A heterogeneous graph cuts algorithm is proposed for difference image analysis. The min-cuts guided by a powerful energy function is implemented to cull the weakly related edges of heterogeneous graph on the difference image. Therefore, a change map possessing smooth inner-regions and clear boundaries can be obtained.

II. MATERIALS AND METHODS

Denote the bi-temporal SAR images as $\mathbf{I}_1$ and $\mathbf{I}_2$. They cover the same geographical region but are observed at different times, t_1 and t_2, respectively. This paper utilizes the heterogeneous graph to comprehensively describe the surface information from SAR images in terms of intensity and structural attributes. Then, the difference image is generated by matching the heterogeneous graphs from the bi-temporal SAR images. Finally, heterogeneous graph cuts algorithm is applied to obtain the change map. The flowchart of the proposed approach is shown in Fig. 1.

A. STRUCTURAL EXTRACTION FROM SAR IMAGE VIA RELATIVE TOTAL VARIATION

In general, an image can be regarded as the superposition of textural component and structural component [30]. Among that, textural component refers to the oscillation of image details such as locally repeated features and fine fragments. Structural component represents the piecewise-constant blocks of images, including contours and homogeneous regions. These components show significantly distinct characteristics during processing and analyzing of images. It is interesting that human vision system has the capacity to understand images while regardless of the textures [31]. Psychological research also shows that human perception usually ignores individual details of an image but focuses on its overall structural features [32]. For a SAR image, its inherent speckle noise can be regarded as a kind of irregular texture. Based on above analysis, the relative total variation (RTV) approach is employed to extract structural component from a SAR image in the presence of complex texture (speckle noise), and apply it to change detection tasks.

In the RTV model, the structural image $\mathbf{S}$ is acquired via solving the following objective function:

$$\underset{\mathbf{s}}{\operatorname{argmin}} \sum_{i=1}^{N} (S_i - I_i)^2 + \lambda \cdot \left(\frac{D_x(i)}{L_x(i) + \varepsilon} + \frac{D_y(i)}{L_y(i) + \varepsilon} \right) \quad (1)$$

where $\mathbf{I}$ is the input SAR image and N is its total number of pixels. λ is a free parameter to tune the smoothness of RTV. ε is a small positive number to avoid the denominator being zero. The former term of the function ensures that the input SAR image $\mathbf{I}$ and output structural image $\mathbf{S}$ are as similar as possible, and the latter one makes sure that the textures can be removed with main structures retained.

In detail, D_x and D_y are the windowed total variations along the x and y axes, respectively. They represent the absolute variations of the local window $R(i)$, and can be calculated by

$$D_x(i) = \sum\nolimits_{j \in R(i)} g_{i,j} \cdot \left| (\partial_x \mathbf{S}) j \right| \quad (2)$$

$$D_y(i) = \sum\nolimits_{j \in R(i)} g_{i,j} \cdot \left| (\partial_y \mathbf{S}) j \right| \quad (3)$$

where j represents a neighbor around pixel i within the window $R(i)$. $\partial_x \mathbf{S}$ and $\partial_y \mathbf{S}$ are respectively the partial derivatives along x and y directions in the structural image $\mathbf{S}$. $g_{i,j}$ is the two-dimensional Gaussian kernel function for weighting, and can be expressed as

$$g_{i,j} = \exp\left\{ -\frac{(x_i - x_j)^2 + (y_i - y_j)^2}{2\sigma^2} \right\} \quad (4)$$

where parameter σ is the variance of the window $R(i)$.

Differently, L_x and L_y represent the windowed inherent variations along x and y directions, respectively, and they capture the overall variations. They can be calculated by

$$L_x(i) = \sum\nolimits_{j \in R(i)} \left| g_{i,j} \cdot (\partial_x \mathbf{S}) j \right| \quad (5)$$

$$L_y(i) = \sum\nolimits_{j \in R(i)} \left| g_{i,j} \cdot (\partial_y \mathbf{S}) j \right| \quad (6)$$

The separated structural component of SAR image, $\mathbf{S}$, can be obtained via minimizing (1). More detailed solution procedures are available in [32].

B. HETEROGENEOUS GRAPH CONSTRUCTION BASED ON INTENSITY AND STRUCTURAL ATTRIBUTES

Heterogeneous graph, containing diversified types of vertices and edges, are capable of integrating different attributes and describing multiple relationships [33]. Therefore, this paper takes advantage of the heterogeneous graph to jointly express the characteristics of intensity and structural attributes from SAR image, and carry out change detection research.

The intensity and structural attributes are incorporated into vertices, and the vertices are closely connected, thereby heterogeneous graph can be constructed. Formally, denote $\mathbf{HG} = \{\mathbf{V}, \mathbf{E}_{\mathrm{II}}, \mathbf{E}_{\mathrm{SS}}, \mathbf{E}_{\mathrm{IS}}, \mathbf{E}_{\mathrm{SI}}, \boldsymbol{\omega}_{\mathrm{II}}, \boldsymbol{\omega}_{\mathrm{SS}}, \boldsymbol{\omega}_{\mathrm{IS}}, \boldsymbol{\omega}_{\mathrm{SI}}\}$ as heterogeneous graph, then it can be represented as:

$$\mathbf{V} = \mathbf{I} \cup \mathbf{S}; |\mathbf{V}| = 2N \quad (7)$$

$$\mathbf{E}_{\mathrm{II}} = \left\{ (I_p, I_q); I_q \in CN(I_p) \right\} \quad (8)$$

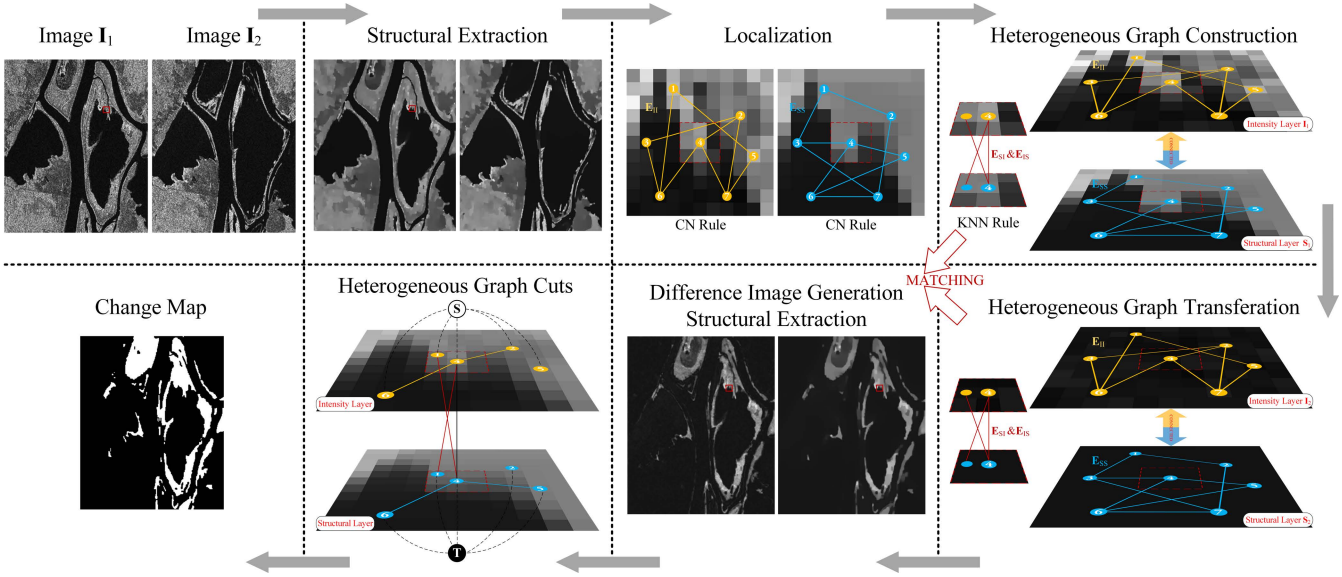

FIGURE 1. Flowchart of the proposed graph-driven approach.

$$\mathbf{E}_{\mathrm{SS}} = \left\{(S_p, S_q);\, S_q \in CN(S_p)\right\} \tag{9}$$

$$\mathbf{E}_{\mathrm{IS}} = \left\{(I_p, S_q);\, S_q \in S_p \cup \mathrm{KNN}(S_p)\right\} \tag{10}$$

$$\mathbf{E}_{\mathrm{SI}} = \left\{(S_p, I_q);\, I_q \in I_p \cup \mathrm{KNN}(I_p)\right\} \tag{11}$$

where $\mathbf{V}$ represents the vertex set, which consists of the pixels from both SAR image $\mathbf{I}$ and the extracted structural component $\mathbf{S}$. I_p is an intensity vertex located at the position (x, y), so is Sp as a structural vertex. $\mathrm{KNN}(I_p)$ represents the set of adjacent vertices around I_p under the K nearest neighbor rule in spatial domain. $\mathrm{CN}(I_p)$ is the set of coupling neighborhood [34] around I_p, and can be obtained by

$$\mathrm{CN}(I_p) = \left\{N_{1<n,M>}(I_p) \cup N_{2<n,M>}(I_p)\right\} \tag{12}$$

where $N_{1<n,M>}(I_p)$ represents the M most similar neighbours around vertex I_p within $n \times n$ window from the first SAR image, so is $N_{2<n,M>}(I_p)$ from the second SAR image

$\mathbf{E}_{\mathrm{II}}$ represents the intra-connection of intensity vertices. In order to reduce the interference of speckle noise, the non-iteration probabilistic patch-based weight [35] is introduced to quantify the intra-connections. Then, the ω_{II} is calculated via comparing the two patches around the vertices I_p and I_q, and can be expressed as:

$$\omega_{\mathrm{II}}(I_p, I_q) = \exp\left\{-\frac{1}{k}\sum \log\frac{1}{2}\left(\frac{I_{p,k}}{I_{q,k}} + \frac{I_{q,k}}{I_{p,k}}\right)\right\} \tag{13}$$

where $I_{p,k}$ and $I_{q,k}$ are the k-connected neighbours in the two patches, respectively.

$\mathbf{E}_{\mathrm{SS}}$ represents the intra-connection of structural vertices. Since the speckle noise is removed by RTV model, the weight ω_{SS} is computed by one-dimensional Gaussian kernel function:

$$\omega_{\mathrm{SS}}(S_p, S_q) = \exp\left\{-\frac{\|S_p - S_q\|^2}{2\sigma^2}\right\} \tag{14}$$

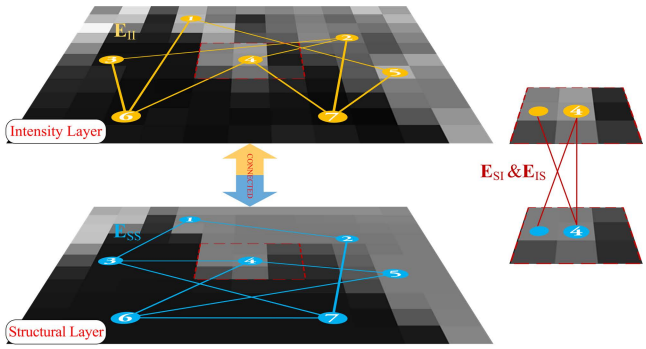

FIGURE 2. The diagram of heterogeneous graph.

where σ represents the standard deviation of the $\mathrm{KNN}(S_p)$ set in the structural layer.

$\mathbf{E}_{\mathrm{IS}}$ and $\mathbf{E}_{\mathrm{SI}}$ represent the inter-connection of the different attribute vertices, and the weights ω_{IS} and ω_{SI} are defined as:

$$\omega_{\mathrm{IS}}(I_p,\ S_q) = \beta \tag{15}$$

$$\omega_{\mathrm{SI}}(S_p,\ I_q) = \frac{1}{\beta} \tag{16}$$

where β is a bias parameter to adjust the predominance of attributes, and is often set to 1 to represent the equilibrium of attribute utilization.

A simple example of heterogeneous graph is given in Fig. 2. In summary, we construct heterogeneous graph with two types of edges (intra-connection and inter-connection) under the different neighbor rules, and allocate four kinds of weights to them. Relying on the graph, the complete characteristic information of SAR image can be extracted, which is beneficial for change detection.

C. DIFFERENCE IMAGE GENERATION USING HETERO-GENEOUS GRAPH WITH HYPER-ADJACENCY MATRIX

Within a weighted graph, the adjacency matrix $\mathbf{W}$ is a quantified representation for inner relationships of vertices, being defined as

$$\mathbf{W} = \begin{cases} \omega(p, q), & \forall(p, q) \in \mathbf{E} \\ 0, & \text{otherwise} \end{cases} \tag{17}$$

As the adjacency matrix $\mathbf{W}$ is obtained, the adjacency characteristics of weighted graph can be obtained as follows:

$$(Wf)(p) = \sum_{q \sim p} \omega(p, q) f(p) \tag{18}$$

where $\boldsymbol{f} = \{f(p), p = 1 \ldots N\}$ is the feature attribute of graph vertices. In a graph, vertices diffuse their information to the neighbors and receive information diffused from others at the same time. Therefore, $Wf(p)$ characterizes the concentration of information from neighboring vertices to the studied vertex p. Further, the characteristic $\mathbf{W}\boldsymbol{f}$ can be also considered as a filtering operator performed in the graph vertex domain, which is promising for speckle suppression. Therefore, the hyper-adjacency matrix $\mathbf{P}$ is presented to describe multiple relationships of heterogeneous graph, and is expressed as:

$$\mathbf{P} = \begin{bmatrix} \mathbf{W}_{\mathrm{I,I}} & \mathbf{W}_{\mathrm{I,S}} \\ \mathbf{W}_{\mathrm{S,I}} & \mathbf{W}_{\mathrm{S,S}} \end{bmatrix} \tag{19}$$

There are two types of edges in the heterogeneous graph, thus the matrix $\mathbf{P}$ contains two types of sub-matrices: intra-adjacency matrices ($\mathbf{W}_{\mathrm{II}}$, $\mathbf{W}_{\mathrm{SS}}$) and inter-adjacency matrices ($\mathbf{W}_{\mathrm{IS}}$, $\mathbf{W}_{\mathrm{SI}}$). Among that, the intra-adjacency matrices indicate the relationships between vertices of intra-connections, and the inter-adjacency matrices express the relationships between the vertices of inter-connections. The values of sub-matrix elements can be acquired according to the four kinds of weights within the heterogeneous graph.

Constructing two heterogeneous graphs with the same topology on bi-temporal SAR images, the change measure can be converted to a match of the multi-attribute vertices and multi-edges within the two graphs. On the basis of hyper-adjacency matrix $\mathbf{P}$, the hyper-adjacency characteristic $\mathbf{Pf}$ is derived to calculate the similarity of heterogeneous graphs:

$$\mathbf{CM} = \max\left\{\left(\left\|\mathbf{P}^{t_1}\mathbf{f}^{t_1}./\mathbf{P}^{t_2}\mathbf{f}^{t_2}\right\|_1\right), \left(\left\|\mathbf{P}^{t_2}\mathbf{f}^{t_2}./\mathbf{P}^{t_1}\mathbf{f}^{t_1}\right\|_1\right)\right\} \tag{20}$$

where $\mathbf{f}^{t1} = [\mathrm{vec}(\mathbf{I}^{t1}), \mathrm{vec}(\mathbf{S}^{t1})]\mathrm{T}$ is the joint attribute vector of the graph vertices, consisting of intensity and structural attributes from the first SAR image, and so is $\mathbf{f}^{t2}$ from the second SAR image. $\mathrm{vec}(\cdot)$ is the operation of converting a matrix into a row vector, and $||\cdot||_1$ represents the L1-norm calculated by regarding the sub-matrices as elements.

D. DIFFERENCE IMAGE ANALYSIS BASED ON HETER-OGENEOUS GRAPH CUTS

After difference image is generated, change detection can be converted to a binary classification problem. Here, the idea of graph cuts [36] are employed to divide the difference image $\mathbf{CM}$ into unchanged and changed regions. A heterogeneous graph $\mathbf{HG}_{\mathrm{CM}}$ is constructed on $\mathbf{CM}$ based on the definition in section II-B. In detail, the heterogeneous cuts (HGC) should be implemented in accordance with the multivariate Gaussian model [37], since each vertex contains both intensity and structural attributes. Therefore, a novel energy function is proposed for optimizing HGC, and can be defined as:

$$\psi(l) = \sum_{p \in \mathbf{V}} D_p(l_p) + \sum_{(p,q) \in \mathbf{E}} U(l_p, l_q) \tag{21}$$

$D_p(\cdot)$ is the data constraint term driven by the observed features, representing the cost to allocate a label l_p (unchanged or changed) to the vertex p. It can be calculated via utilizing the negative log-likelihood

$$D_p(l_p) = -\ln \Pr(z_p|\theta_l) \tag{22}$$

where $z_p = \{I_p, S_p\}$, is a two-dimension feature vector consisting of the intensity and structural attributes. θ_l is a parameter vector of the multivariate generalized Gaussian model associated with label l_p. Pr is the probability that vertex p belongs to label l_p, and can be expressed as

$$\Pr(z_p|\theta_l) = \frac{1}{(2\pi)^{d/2}\left|\sum_l\right|^{1/2}} \times \exp\left(-\frac{1}{2}(z_p - \mu_l)^{\mathrm{T}}\sum\nolimits_l^{-1}(z_p - \mu_l)\right) \tag{23}$$

where d is the dimension of observed features and set to 2. μ denotes the mean vector, and $\sum$ represents the covariance matrix. Both of them can be learned based on the expectation-maximization algorithm [38].

$U(\cdot)$ is the spatial constraint term which penalizes the discontinuity between the labels l_p and l_q, and is expressed as

$$U(l_p, l_q) = \delta(l_p, l_q) Cor(z_p, z_q) \tag{24}$$

$$\delta(l_p, l_q) = \begin{cases} 1, & l_p \neq l_q \\ 0, & l_p = l_q \end{cases} \tag{25}$$

where $Cor(\cdot)$ denotes the correlation between adjacent vectors z_p and z_q. Since the heterogeneous graph has multi-type edges, the $Cor(\cdot)$ can be expressed as:

$$Cor(z_p, z_q) = \sum_{q \in \mathrm{JN}(p)} \omega_{**}(p, q) \tag{26}$$

where $\mathrm{JN}(p)$ is the union of the neighborhood sets $\mathrm{KNN}(p)$ and $\mathrm{CN}(p)$. The ω_{**} derives from the weights of heterogeneous graph, which is defined in (13)-(16). Figure 3 presents a simple diagram to illustrate how to calculate the adjacent correlation $Cor(\cdot)$. In general, the value of $Cor(\cdot)$ depends on the amount and type of edges between the vertices that z_p and z_q correspond to.

The schematic diagram of heterogeneous graph cuts is shown in Fig. 4. Two terminal nodes, T (sink) and S (source), are embed into the heterogeneous graph to represent the

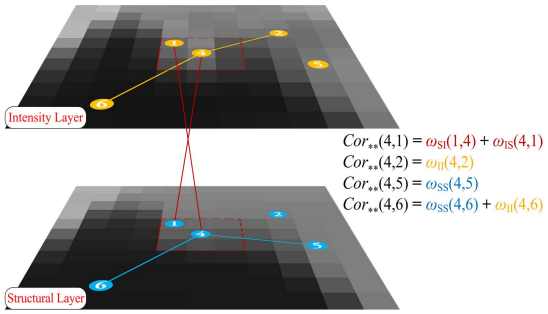

FIGURE 3. The diagram of adjacent correlation *Cor*(·).

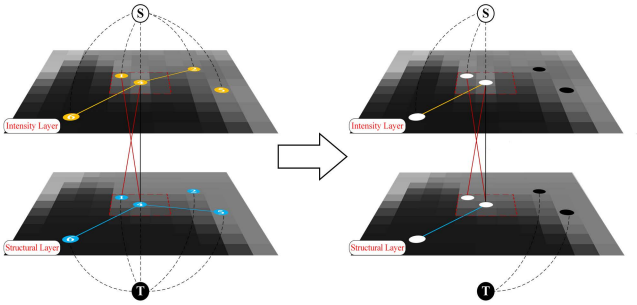

FIGURE 4. The diagram of heterogeneous graph cuts.

unchanged and changed labels, respectively. Therefore, the heterogeneous graph cuts involve two types of links: T-link and N-link. The T-link represents the connection between the vertex and the terminal nodes, and is driven by data term $D_p(\cdot)$. The N-link connects the adjacent vertices and represents the multiple context relationships. The cost of each N-link is assigned by the spatial constraint term $U(\cdot)$, which reflects the correlations of feature vectors for different vertices. The introduced optimization algorithm can automatically seek for the minimal cuts [36].

III. EXPERIMENTAL AND ANALYSIS

In this section, two evaluation experiments based on real SAR datasets are carried out to verify the effectiveness of the proposed graph-driven change detection approach. First, in the forms of grayscale images, the generated difference image is qualitatively compared with the ones derived from MR [13], NR [17], CDI [18], DWT [39] and NLMR [16] approaches. Then, applying the KI threshold [40] to obtain change maps, and validating the performance of six difference image generation approaches through quantitative evaluation. Finally, the PCA-K [41], ITDI-GC [42], MSFCM [43] MRFFCM [44], and PCANet [26] are adopted to comparatively evaluate the effectiveness of the graph-driven change detection approach.

A. EXPERIMENTAL SETUP

The control experiments are conducted here by using the real SAR datasets from different sensors, which are presented in Fig. 5-8. Each SAR dataset contains the bi-temporal images which co-registers at one-pixel level, and the imaging

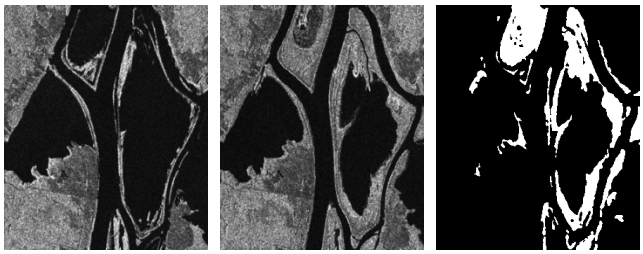

FIGURE 5. Bi-temporal SAR images of Ottawa dataset. (a) Image collected in July 1997. (b) Image collected in August 1997. (c) Ground truth.

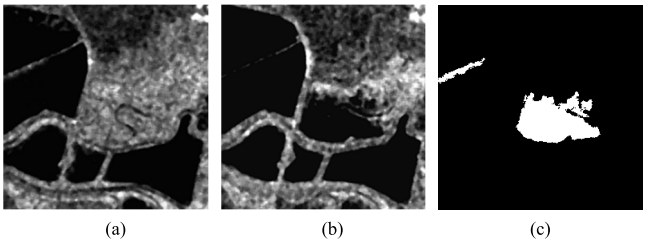

FIGURE 6. Bi-temporal SAR images of San Francisco dataset. (a) Image collected in August 2003. (b) Image collected in May 2004. (c) Ground truth.

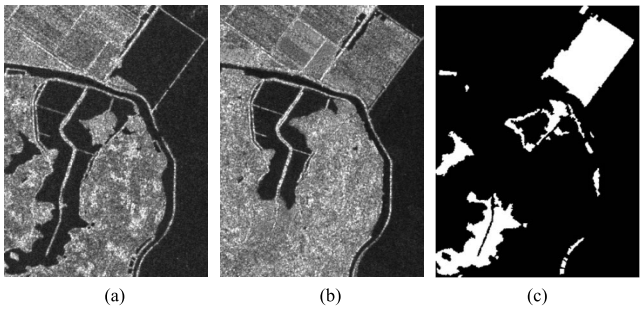

FIGURE 7. Bi-temporal SAR images of Lu'an dataset. (a) Image collected in July 2015. (b) Image collected in October 2015. (c) Ground truth.

information is given in Table 1. The parameter setting is presented as follows. Generically, the parameters of CN are set to $M = 15$ and $n = 7$, and the parameter of KNN is set to $K = 8$. The connected neighbor of ω_{II} is set to $k = 8$ according to [40]. It is recommended to select large values for these parameters when the SAR images show high noise level. The parameters of other approaches are set based on their own articles. Experiments are executed by matrix laboratory 2019 on a machine Intel 3.60 GHz, 16.00 GB memory.

B. EVALUATION CRITERIA

As the datasets have their ground truths, the experimental results can be quantitatively assessed. Denote N as the total number of pixels in the binary ground-truth image. We count the actual number of pixels with regard to the unchanged class (Nu) and the changed class (Nc), respectively. Then, some classic criteria are employed for quantitative analysis:

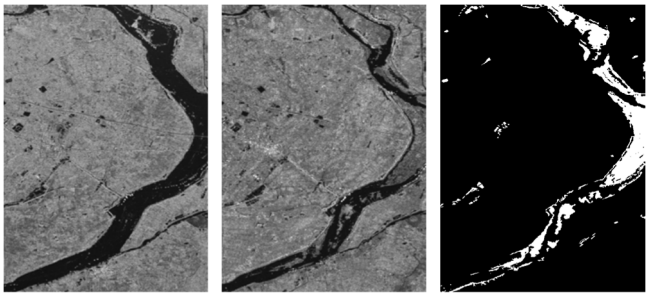

(a) (b) (c)

FIGURE 8. Bi-temporal SAR images of Huai River dataset. (a) Image collected in June 2017. (b) Image collected in September 2017. (c) Ground truth.

TABLE 1. Imaging information of real SAR datasets.

Dataset	Ottawa	San Francisco	Lu'an	Huai River
Sensor	Radarsat-1	ERS-2	Sentinel-1	GaoFen3
Polarization	HH	HH	HV	HH
Resolution	10	20	10	5
Date	Jul. 1997	Aug. 2003	Jul. 2015	Jun. 2017
	Aug. 1997	May. 2004	Oct. 2015	Sep. 2017
Size	290 × 350	256 × 256	429 × 580	554 × 780
Change	Flood event	Land cover	Flood event	Land cover

- true positives (*TP*): the number of changed pixels correctly detected;
- true negatives (*TN*): the number of unchanged pixels correctly detected;
- false positives (*FP*): the number of unchanged pixels that are mistakenly detected as changed ones;
- false negatives (*FN*): the number of changed pixels that are mistakenly detected as unchanged ones;
- false alarm rate (*FA*): the proportion of false positives (*FP*) and the actual unchanged pixels (*Nu*);
- good detection rate (*GD*): the proportion of true positives (*TP*) and the actual changed pixels (*Nc*);

More detail, the percentage correct classification (*PCC*) and kappa coefficient (κ) serve as the criteria for comprehensive evaluation, and the definitions are presented as follows:

$$PCC = TP + TN \tag{27}$$

$$\kappa = \frac{TP + TN - PRE}{1 - PRE} \tag{28}$$

where

$$PRE = \frac{(TP + FP) * Nc + (FN + TN) * Nu}{N^2} \tag{29}$$

C. PERFORMANCE ANALYSIS OF DIFFERENCE IMAGE GENERATION BASED ON HETEROGENEOUS GRAPH

This experiment is conducted to evaluate the validity of the proposed heterogeneous graph (HG) for difference image generation. The first dataset is collected by the RADARSAT sensor in different dates over the Ottawa city. It consists of bi-temporal SAR images, shown in Fig. 5(a) and (b), which reflect the backscattering changes about floods rising and retreating. The difference images generated from the six approaches (MR, NR, CDI, DWT, NLMR and the proposed HG) are presented in Fig. 9. Correspondingly, the change maps obtained by KI thresholding are also exhibited. As observed, the MR and NR approach generate messy difference images, and thus the change maps present many spots in the unchanged regions. The NLMR gives a smooth change measure results, but the pixels located at the edges of the changed regions present low intensity, resulting in the miss detection. The result of DWT also lacks accuracy in the boundary areas since the difference image is coarse. The change measure results of CDI and HG are satisfactory as their difference images appear a good separability. Moreover, in the changed regions, there is a large overlap between the change map of HG and the ground truth. The quantitative estimation for the six change maps is shown in Table 2. The proposed HG approach shows the lowest false negative, just 535. Meanwhile, the criteria of *PCC* and κ are superior to others.

The second dataset consists of bi-temporal SAR images observed by European Remote Sensing satellite over the San Francisco city. Some areas are newly irrigated, causing the changes of backscatter in SAR images, which show in Fig. 6(a) and (b). Six difference images are exhibited in Fig. 10. Among them, the images of MR, NR, DWT and NLMR all present three main partitions, including unchanged land, unchanged water and changed irrigation areas. Due to that these approaches take the ratio operator as the inner-kernel to measure changes, the differences of low-intensity areas are amplified. The unchanged water areas are thus mistakenly highlighted, generating unsatisfactory difference images. Intuitively, different amounts of spots appear in the background area of their change maps, as Fig. 10(a), (b), (d) and (e) show. The CDI and HG approaches overcome above problems respectively by combining different operators or introducing multiple attributes, making their difference images show specific binarization trends. Meanwhile, the difference image derived from the proposed HG is flatter than that from CDI in unchanged land areas, as shown in Fig. 10(c) and (f). The corresponding change map of HG is, of course, most similar to the ground truth. Table 3 presents the quantitative results of six change measure approaches. The HG clearly outperforms other ones in term of all criteria.

The third dataset is observed by the Sentinel-1A sensor. The contained bi-temporal SAR images describe surface changes around the Lu'an City. The results of six change measure approaches are shown in Fig. 11. It is easy to see that the change maps of MR, NR, CDI and DWT all contain many isolate spots, this is because the background areas of their difference images are chaotic. The NLMR approach is good at exhibiting regional integrity but poor at boundary description, so it gets a high miss detection. The proposed approach

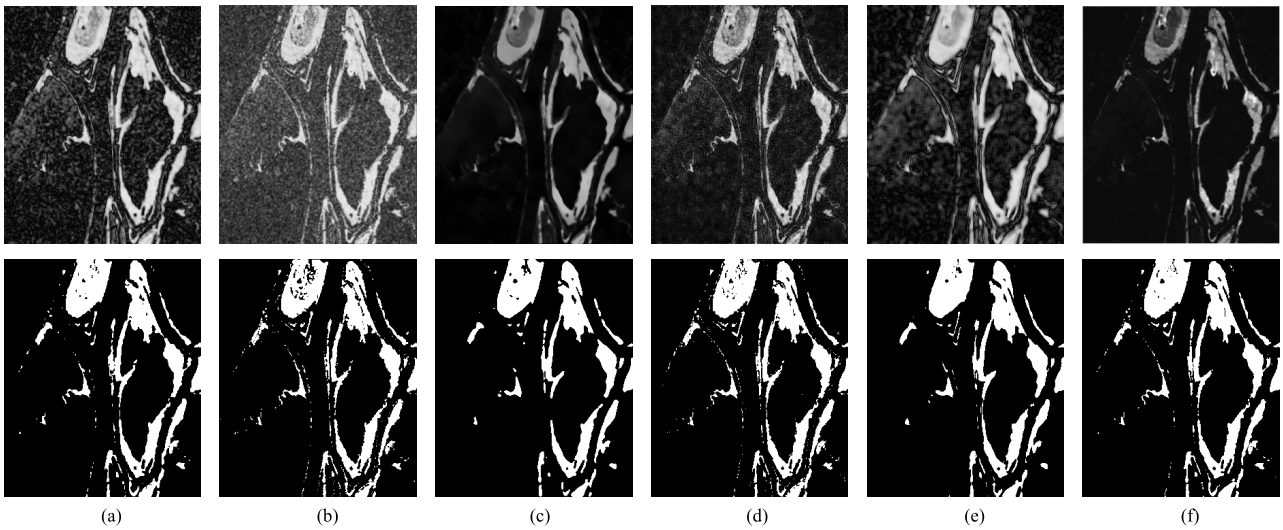

FIGURE 9. Difference images (first row) and change maps (second row) of six change measure approaches on Ottawa dataset. (a) MR (b) NR. (c) CDI. (d) DWT. (e) NLMR. (f) HG.

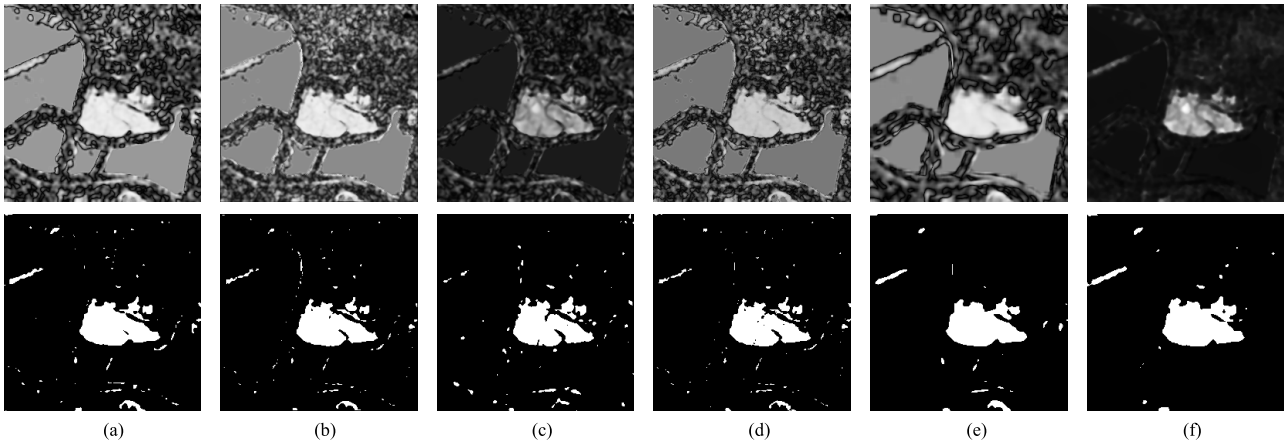

FIGURE 10. Difference images (first row) and change maps (second row) of six change measure approaches on San Francisco dataset. (a) MR (b) NR. (c) CDI. (d) DWT. (e) NLMR. (f) HG.

TABLE 2. Results of change measure on Ottawa datasets.

Method	FN	FP	PCC	κ	Time/s
MR	1361	1407	0.9727	0.8977	1.35
NR	1600	778	0.9766	0.9101	5.41
CDI	1603	484	0.9794	0.9205	8.39
DWT	894	949	0.9818	0.9319	6.53
NLMR	1389	772	0.9787	0.9188	2.04
HG	535	909	0.9858	0.9471	24.46

TABLE 3. Results of change measure on san Francisco datasets.

Method	FN	FP	PCC	κ	Time/s
MR	516	861	0.9790	0.8470	1.12
NR	757	604	0.9792	0.8412	3.71
CDI	762	832	0.9757	0.8181	5.67
DWT	786	604	0.9788	0.8373	4.89
NLMR	402	667	0.9837	0.8803	1.92
HG	215	542	0.9884	0.9157	21.32

can generate a difference image with good separability, and the change map can reflect real changes, as the visual effect of background area is suppressed. In quantitatively, the proposed HG approach gains the lowest *FP* and the highest κ.

The Huai River dataset is collected by the GaoFen-3 SAR sensor at different periods, which shown in Fig. 8. The contained bi-temporal SAR images describe the changes of land-cover around Huai River in the flood and dry seasons, respectively. The difference images and change maps obtained by the six experimental approaches are exhibited in Fig. 12(a)-(e). As can be seen that the unchanged areas in MR, NR and DWT are uneven, which cannot distinguish

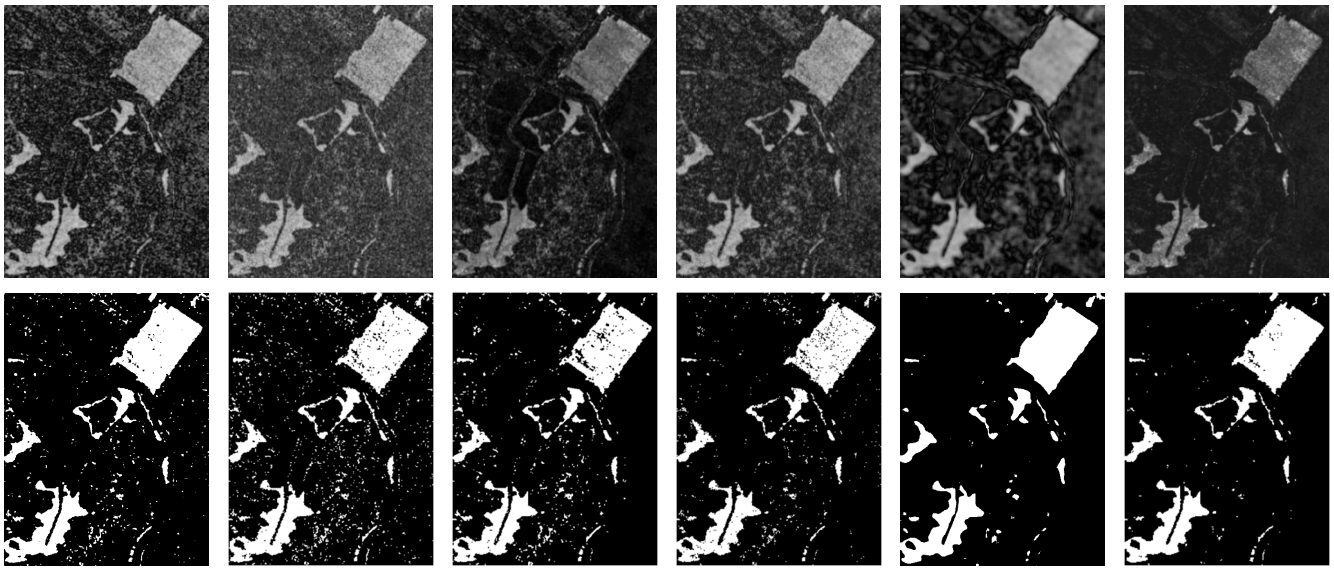

FIGURE 11. Difference images (first row) and change maps (second row) of six change measure approaches on Lu'an dataset. (a) MR (b) NR. (c) CDI. (d) DWT. (e) NLMR. (f) HG.

TABLE 4. Results of change measure on Lu'an datasets.

Method	FN	FP	PCC	κ	Time/s
MR	3966	5044	0.9638	0.8610	1.42
NR	3830	8887	0.9489	0.8118	10.74
CDI	5185	4912	0.9594	0.8419	16.21
DWT	5591	3312	0.9642	0.8575	11.67
NLMR	4131	2548	0.9732	0.8939	4.32
HG	3859	992	0.9805	0.9218	43.12

TABLE 5. Results of change measure on Huai River datasets.

Method	FN	FP	PCC	κ	Time/s
MR	4233	6044	0.9758	0.8361	1.65
NR	3406	8821	0.9712	0.8141	18.18
CDI	4786	5606	0.9755	0.8320	24.61
DWT	5535	4486	0.9764	0.8338	19.34
NLMR	4044	6405	0.9754	0.8346	6.57
HG	5424	2472	0.9814	0.8654	89.52

the unchanged and changed regions very well. Therefore, many unchanged pixels are incorrectly detected as changed ones, resulting a high false detection. The result of NLMR approach, shown in Fig. 12(e), is too smooth to accurately describe the details of changed areas. The unchanged areas in the difference image of CDI appear to be flat, while the changed areas are dim. In Fig. 12(e), the difference image generated by HG shows good separability, despite it is a little bit dark. In the aspect of quantitative analysis, the change map generated from HG is superior to the ones from other approaches, especially in the criteria of FP and κ. These results affirm the performance of HG approach in measuring changes.

In fact, the proposed HG always gets the most time cost due to the complexity of the heterogeneous graph, but it seems acceptable considering the improvement of change detection accuracy.

TABLE 6. Results of change detection on Ottawa datasets.

Method	FN	FP	PCC	κ	Time/s
PCA-K	1529	979	0.9753	0.9059	2.47
MSFCM	1455	1099	0.9748	0.9046	24.15
MRFFCM	712	1636	0.9769	0.9151	17.21
ITDI-GC	1228	599	0.9820	0.9335	15.17
PCANet	951	905	0.9817	0.9312	931.68
HGC	741	450	0.9883	0.9556	38.53

D. PERFORMANCE ANALYSIS OF CHANGE DETECTION BASED ON HETEROGENEOUS GRAPH CUTS

A contrastive analysis among heterogeneous graph cuts (HGC), PCA-K, MSFCM, MRFFCM, ITDI-GC and PCANet approaches is carried out in the second experiment, aiming to verify the performance of HGC for change detection tasks. Six change maps of Ottawa dataset are shown in Fig. 13, and the quantitative criteria are exhibited in Table 6. The change map of PCA-K is smooth enough with less occurrence of isolated pixels. Nevertheless, its changed regions within the red box are patchy, which results in a high miss detection. The MRFFCM presents coarse results around the boundary, causing high false detection. In contrast, the ITDI-GC approach presents overly smoothness, so that the small unchanged regions are corroded, which shown in Fig. 13(d). Excessive

TABLE 7. Results of change detection on san Francisco datasets.

Method	FN	FP	PCC	κ	Time/s
PCA-K	715	201	0.9860	0.8891	2.81
MSFCM	481	357	0.9872	0.9025	13.52
MRFFCM	226	1112	0.9796	0.8587	15.35
ITDI-GC	693	228	0.9859	0.8891	9.57
PCANet	239	519	0.9884	0.9152	831.68
HGC	319	367	0.9895	0.9215	31.03

TABLE 8. Results of change detection on Lu'an datasets.

Method	FN	FP	PCC	κ	Time/s
PCA-K	5579	877	0.9741	0.8938	3.31
MSFCM	2938	2593	0.9778	0.9139	62.33
MRFFCM	1777	6311	0.9675	0.8797	23.71
ITDI-GC	3430	857	0.9828	0.9311	24.82
PCANet	9919	88	0.9598	0.8252	1231.68
HGC	2719	778	0.9859	0.9442	65.43

TABLE 9. Results of change detection on Huai River datasets.

Method	FN	FP	PCC	κ	Time/s
PCA-K	5190	3768	0.9789	0.8506	4.71
MSFCM	4349	3674	0.9811	0.8676	97.62
MRFFCM	2978	9085	0.9716	0.8181	34.82
ITDI-GC	5540	3724	0.9782	0.8447	35.58
PCANet	10565	508	0.9739	0.7898	1823.12
HGC	3850	3800	0.9820	0.8749	123.35

TABLE 10. Ablative experiment results on Ottawa dataset.

Method	FN	FP	PCC	κ
MR-KI	1361	1407	0.9727	0.8977
MR-GC	1328	1359	0.9735	0.9006
MR-HGC	1027	1242	0.9776	0.9165
HG-KI	535	909	0.9858	0.9471
HG-GC	901	457	0.9866	0.9492
HG-HGC	741	450	0.9883	0.9556

boundary changes are detected by the MSFCM approach, thus reducing the accuracy. The change maps of PCANet and HGC can reflect most changes, while the map of HGC is more approximate to the ground truth than that of PCANet. From the statistics, the proposed HGC shows an outstanding performance compared with other approaches.

Figure 14 gives the results of six approaches on San Francisco dataset. The change map MRFFCM presents many spots in the unchanged areas. The changed regions of PCANet result is fine but some spots are appeared in the unchanged regions. The PCA-K, MSFCM, ITDI-GC and HGC approaches are capable of speckle suppression as their change maps show regional integrity in both changed and unchanged regions. However, the results of PCA-K and ITDI-GC present a tendency of high miss-detection, the result of HGC shows an equilibrium between *FN* and *FP*. From Table 7, the highest κ is acquired by HGC, which can manifest its superiority.

The change detection results on Lu'an dataset are exhibited in Fig. 15 and Table 8. The change map of MRFFCM is dizzying, since many isolated pixels are incorrectly detected in unchanged regions. The results of PCA-K, MSFCM and ITDI-GC are flat, except for the slightly appeared miss-detection in the upper right changed regions. The PCANet approach appears an extreme bias on the Lu'an dataset, resulting in a very high miss-detection. In the traditional unsupervised pattern, HGC produces a satisfactory change detection result. The integrality of changed region and the smoothness of unchanged region are both appeared in its change map, and thus HGC gains the highest criteria κ.

Six change maps of Huai River dataset are presented in Fig. 16. The results of MRFFCM is poor, since its change map is messy. Many unchanged pixels are misidentified as changed ones. In contrast, the change maps of PCA-K, MSFCM and ITDI-GC show flat areas, obtaining less false detections. A similar bias of PCANet approach also appears on the Huai River dataset. This shows the instability of automatic samples labeling. The proposed HGC approach presents the ability of accurate detection at the river bed boundaries. From Table 9, the highest κ is gained by HGC, verifying the effectiveness of the proposed graph-driven strategy.

E. ABLATIVE EXPERIMENT

This experiment is conducted to evaluate the independent performance of the proposed heterogeneous graph cuts. Ablative experiments on Ottawa dataset through MR-KI (MR difference image with KI threshold), MR-GC (MR difference image with traditional graph cuts), MR-HGC (MR difference image with heterogeneous graph cuts), HG-KI (HG difference image with KI threshold), HG-GC (HG difference image with traditional graph cuts) and HG-HGC (HG difference image with heterogeneous graph cuts) approaches are carried out. The qualitative and quantitative evaluations are presented in Fig. 17 and Table 10, respectively. It is observed that GC and HGC gain smoother and more accurate results than KI threshold on both MR and HG difference images. Meanwhile, the κ of HGC is higher than GC. This proves a better performance of HGC for difference image analysis. However, the results of MR-HGC are still lower than those of HGC-KI. It indicates that the difference image generation based on HG contributes more to improving the accuracy of change detection in this study.

IV. DISCUSSION

Scholars usually improve the performance of change detection approaches from two aspects: change measure and change analysis. Among that, the core issue of change measure is how to reduce speckle noise and accurately describe

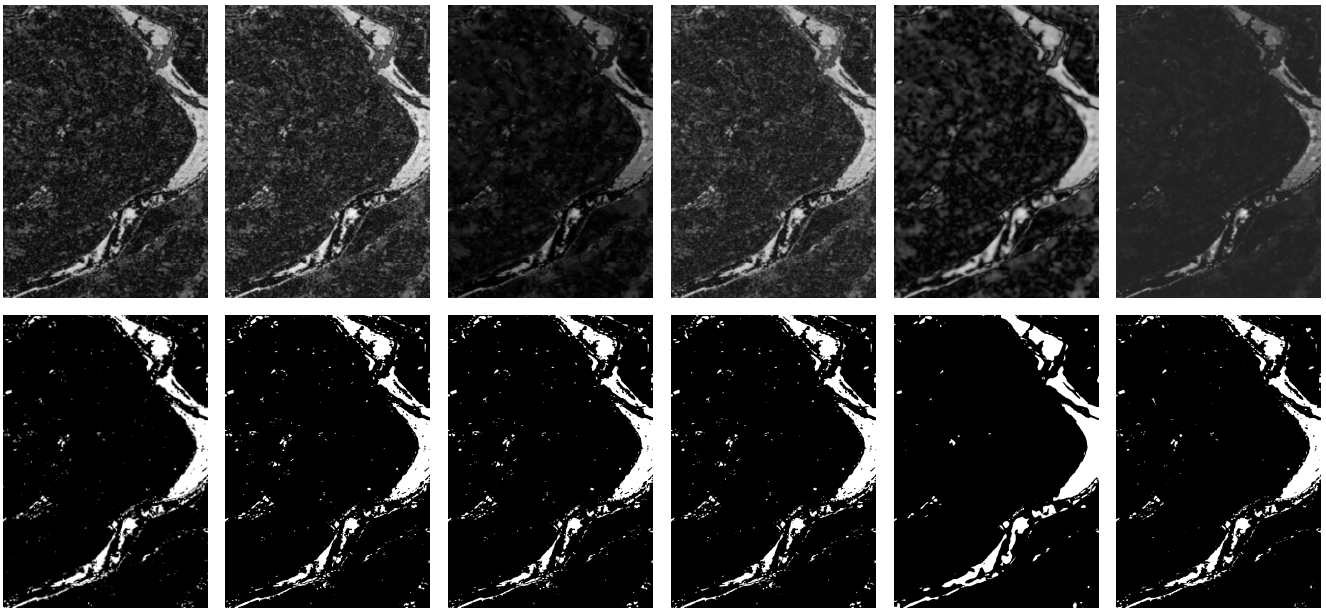

FIGURE 12. Difference images (first row) and change maps (second row) of six change measure approaches on Huai River dataset. (a) MR (b) NR. (c) CDI. (d) DWT. (e) NLMR. (f) HG.

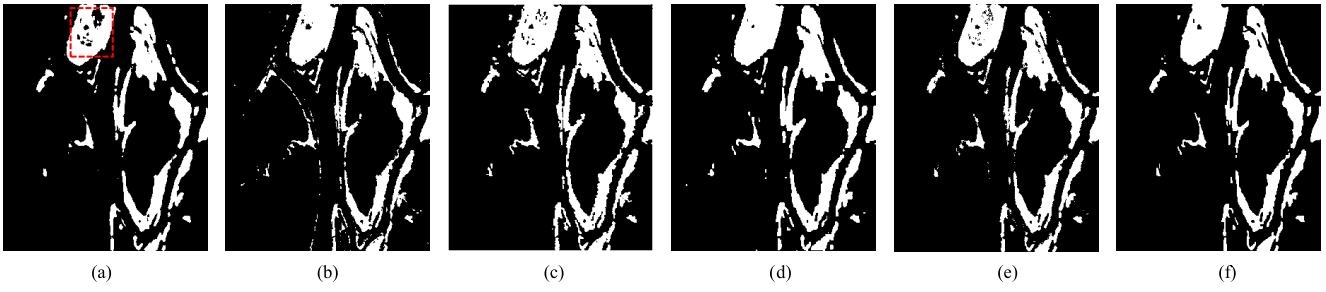

FIGURE 13. Change maps of experimental approaches on Ottawa dataset. (a) PCA-K. (b) MSFCM. (c) MRFFCM. (d) ITDI-GC. (e) PCANet. (f) HGC.

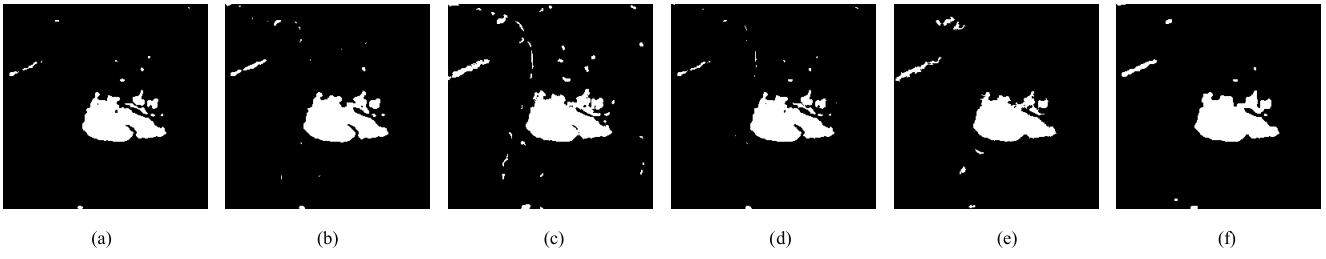

FIGURE 14. Change maps of experimental approaches on San Francisco dataset. (a) PCA-K. (b) MSFCM. (c) MRFFCM. (d) ITDI-GC. (e) PCANet. (f) HGC.

the change level simultaneously. Inspired by the filtering strategy, some approaches, such as MR, NR and NLMR, take advantage of local pixels or patches to smoothly measure changes. Moreover, other approaches, like CDI and DWT, employ the comprehensive information from different operators or attributes to optimize the description of changes. The proposed approach combines both of the above strategies by introducing heterogeneous graph, in which the intensity and structural attributes are integrated into vertices, and the multiple relationships of these attributes are defined as two type of edges. These attributes describe the surface information from different aspects, leading to improved perception of changes. Furthermore, a global filtering is constructed in the graph domain by the hyper-adjacency characteristic derived from multiple relationships, thereby suppressing speckle noise effectively. Therefore, the proposed HG approach can

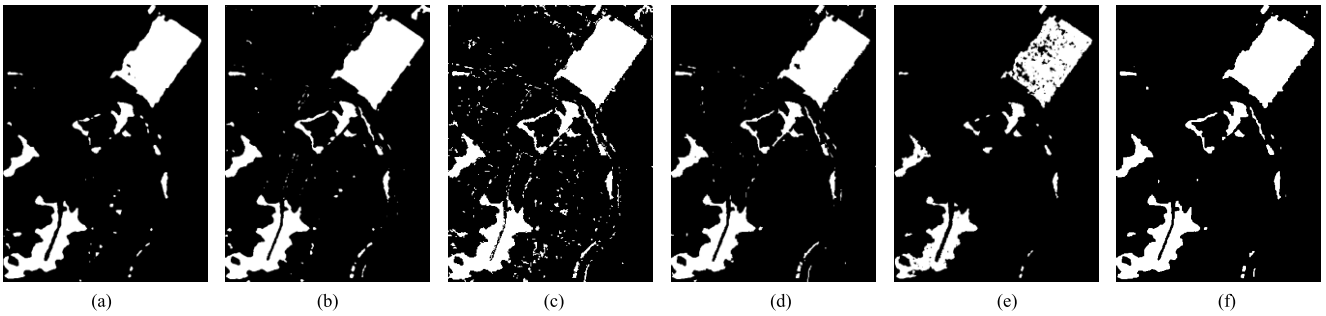

FIGURE 15. Change maps of experimental approaches on Lu'an dataset. (a) PCA-K. (b) MSFCM. (c) MRFFCM. (d) ITDI-GC. (e) PCANet. (f) HGC.

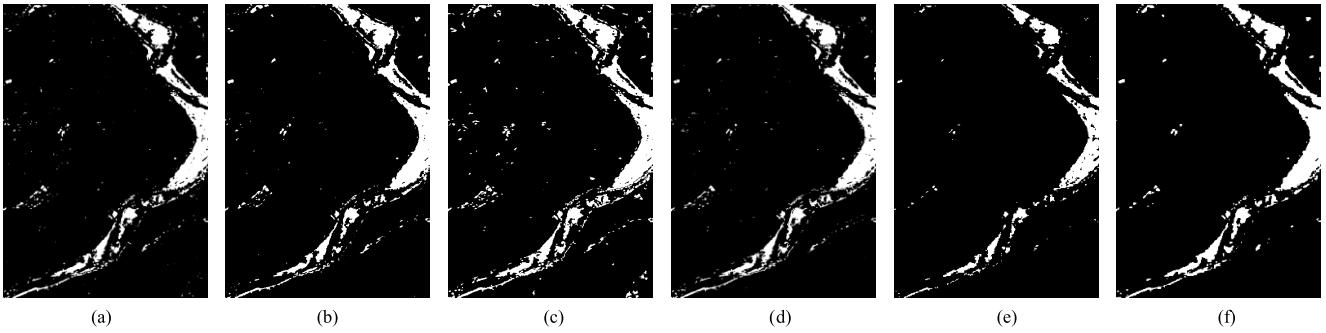

FIGURE 16. Change maps of experimental approaches on Huai River dataset. (a) PCA-K. (b) MSFCM. (c) MRFFCM. (d) ITDI-GC. (e) PCANet. (f) HGC.

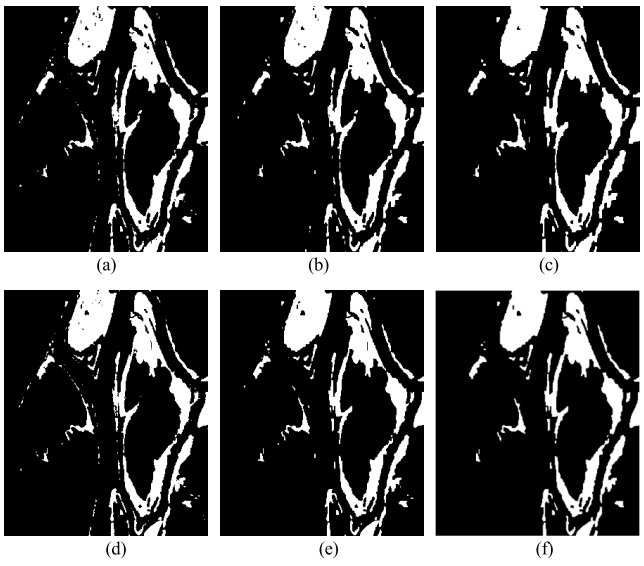

FIGURE 17. The independent performance analysis of heterogeneous graph cuts on Ottawa dataset. (a) MR-KI. (b) MR-GC. (c) MR-HGC. (d) HG-KI. (e) HG-GC. (f) HG-HGC.

generate the difference image with good separability, which has been proved in section 3. Here, the FA and GD are set as the horizontal and vertical axes, and plot the receiver operating characteristic (ROC) curves [45], in order to completely evaluate the difference images at different thresholds. In general, the bigger is the area under the curve, the better is the separability of the approach represented by the curve. The ROC curves for all experimental approaches and datasets are shown in Fig. 18. It can observe that the proposed HG (red one) considerably outperforms other ones. It means that the change measure strategy based on heterogeneous graph is more effective than those based on other approaches at any thresholds.

As the post-processing of change measure, the core task of change analysis is to ensure that the flatness of unchanged regions and the integrity of changed regions in the final change map. This requests for an unbiased and stable change detection approach. We present the statistics charts of FN, FP, PCC and κ for all approaches based on the four datasets, as shown in Fig. 19. The MSFCM and MRFFCM approaches are biased toward higher false detection both on the Lu'an and Huai River datasets. Their means of FP are respectively 1930 and 4536, higher than other approaches, indicating an insufficient performance in anti-noise. The PCA-K and ITDI-GC approaches appear over-smoothed, showing biases toward high miss detection. The PCANet approach shows marked instability, as it exhibits extreme biases on the Lu'an and Huai river datasets while performs well on other datasets. This is probably due to the lack of accuracy for the automatically generated samples. For change detection tasks, the key problem to be solved for the approaches like PCANet is to free the classifier from its dependence on sample annotations. The proposed HGC approach is stable and unbiased because of the introduction of multi-attributes and multi-relationships, and it gets balanced FN and FP values on

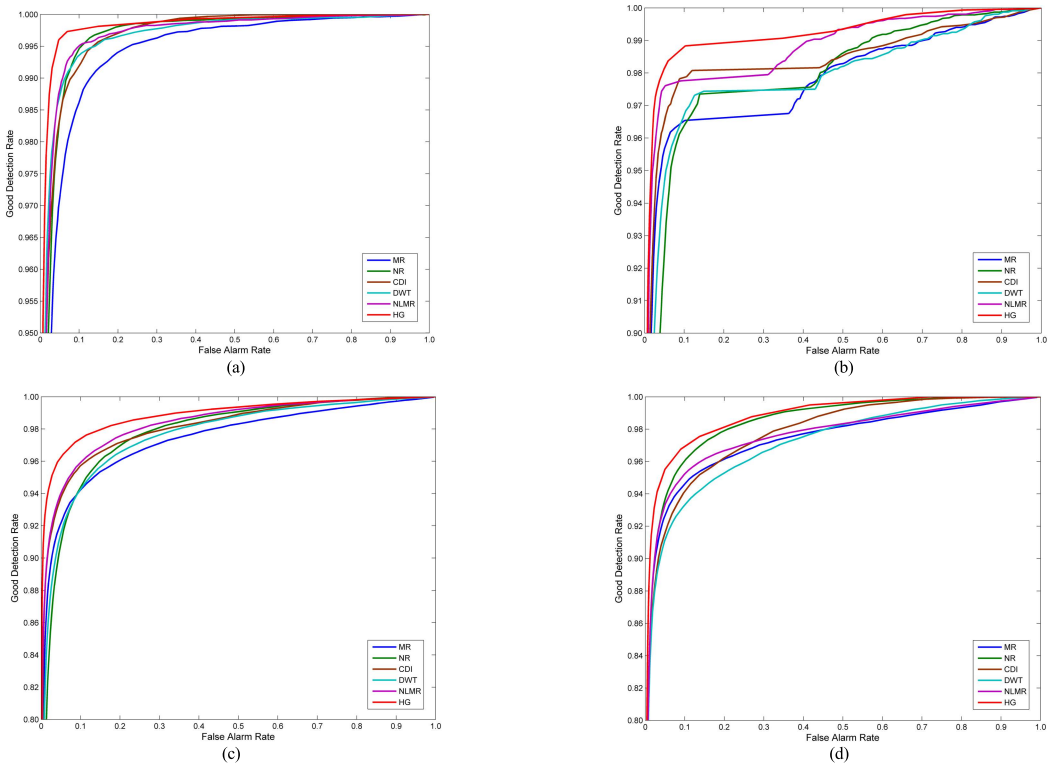

FIGURE 18. The performance analysis of different change measure approaches on four SAR datasets. (a) Ottawa. (b) San Francisco. (c) Lu'an. (d) Huai River.

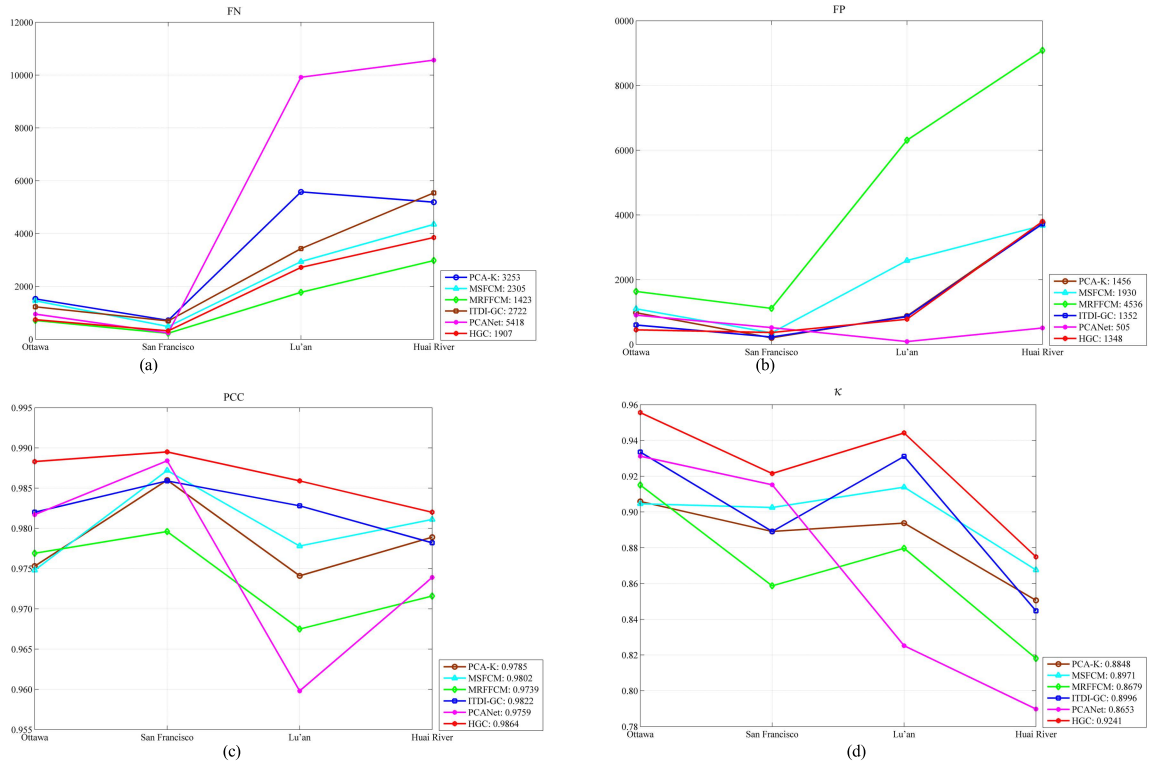

FIGURE 19. The performance analysis of different change detection approaches on four SAR datasets. (a) FP; (b) FN; (c) PCC; (d) κ.

the four experimental datasets, leading to the highest *PCC* and κ. These are powerful proofs for the effectiveness of our proposed approach.

In section II-B, the heterogeneous graph is constructed based on the coupling neighborhood and the K nearest neighbor rules. The parameter M controls the connections of

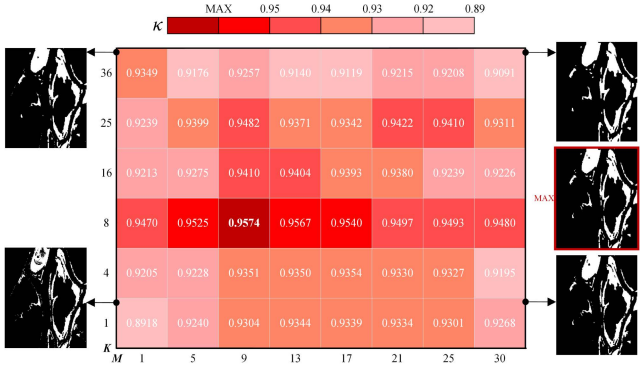

FIGURE 20. Kappa coefficient of the proposed HGC for different K and M on the Ottawa dataset (ENL = 12.5 and 12.6).

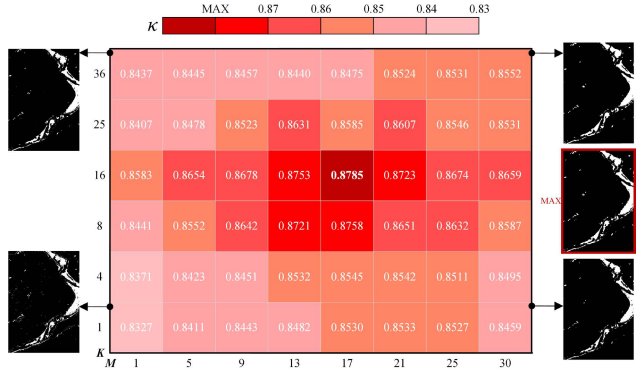

FIGURE 21. Kappa coefficient of the proposed HGC for different K and M on the Huai River dataset (ENL = 3.12 and 2.62).

vertices in the same layer. Therefore, it can decide the structure of the heterogeneous graph and affect the results of change detection. If the parameter M is assigned with a smaller value, the overall relevance of vertices in the same layer would become lower. The resultant less information of neighboring vertices reflected by hyper-adjacency characteristics would lead to a weakened anti-noise performance for the HGC approach. The parameter K possesses similar properties to M, except that it controls the connections of vertices from different layers. For further analysis, K is set to 1, 4, 8, 16, 25, 36, and M is set to 1, 5, 9, 13, 17, 21, 25, 30 to test the fluctuations of κ on Ottawa and Huai River datasets, respectively. The results are shown in Fig. 20 and Fig. 21. Each square represents the value of κ under the corresponding parameters. It can be observed that the κ rises first and then falls in both of the two charts. The lowest κ always appears at the bottom left corner ($K = 1$ and $M = 1$), and their corresponding change maps exist many spots in the unchanged areas. The κ values of the upper right squares are also unsatisfactory as their change maps are over-smoothing. For the Ottawa dataset, the highest κ appears when $K = 8$ and $M = 9$, and its surrounding κ values are also decent. In general, $K = 8$ and M in the range of 5 to 17 are beneficial for the proposed HGC approach to detect the changes of Ottawa dataset. For the Huai River dataset, the highest κ appears when $K = 16$ and $M = 17$. The optimum value range for K is 8 to 16, and the range for M is 13 to 21, indicating that large K and M are more suitable for detecting the changes of Huai River dataset. Considering the equivalent number of looks (ENL) of these two datasets, large values are suggested for these parameters when the SAR images show high noise level.

V. CONCLUSION

In this paper, a heterogeneous graph with a dual-layer structure is proposed for SAR image change detection. The graph can describe the surface information of SAR images in terms of intensity and structural attributes. Meanwhile, the hyper-adjacency matrix is designed to quantify the multi-relationships of different attributes. The change measure is implemented by comparing the derived hyper-adjacency characteristics of bi-temporal SAR images, and thus generating the difference image with good separability. Finally, heterogeneous graph cuts algorithm is presented to obtain the change map through cutting off the weakly related edges of heterogeneous graph on the difference image. Experiments based on four real SAR images are performed to validate the effectiveness of the proposed approach. Qualitative and quantitative analyses manifest that our proposed graph-driven change detection approach outperforms other state-of-art approaches. Furthermore, ablative experiment indicates that heterogeneous graph-based difference image generation makes a greater contribution to improving the accuracy of change detection.

In fact, there exists the scalability problem for the proposed graph-driven change detection approach, since the size of hyper-adjacency matrix is proportional to the number of vertices N and the dimension of attributes Q. The computational time could become longer when the number of vertices or attributes increases. Thus, the computational complexity of the HGC approach is $O\{(QN)^2\}$. There are some ways to alleviate this problem, such as the factorization of hyper-adjacency matrix or the introduction of superpixel. The scalability issue will be addressed in future works.

REFERENCES

[1] S. Grimaldi, J. Xu, Y. Li, V. R. N. Pauwels, and J. P. Walker, "Flood mapping under vegetation using single SAR acquisitions," *Remote Sens. Environ.*, vol. 237, Feb. 2020, Art. no. 111582.

[2] D. Liang, H. Guo, L. Zhang, Y. Cheng, Q. Zhu, and X. Liu, "Time-series snowmelt detection over the Antarctic using Sentinel-1 SAR images on Google Earth engine," *Remote Sens. Environ.*, vol. 256, Apr. 2021, Art. no. 112318.

[3] V. Akbari, A. P. Doulgeris, and T. Eltoft, "Monitoring glacier changes using multitemporal multipolarization SAR images," *IEEE Trans. Geosci. Remote Sens.*, vol. 52, no. 6, pp. 3729–3741, Jun. 2014.

[4] M. Manzoni, A. Monti-Guarnieri, and M. E. Molinari, "Joint exploitation of spaceborne SAR images and GIS techniques for urban coherent change detection," *Remote Sens. Environ.*, vol. 253, Feb. 2021, Art. no. 112152.

[5] H. Zhang, H. Lin, and Y. Li, "Impacts of feature normalization on optical and SAR data fusion for land use/land cover classification," *IEEE Geosci. Remote Sens. Lett.*, vol. 12, no. 5, pp. 1061–1065, May 2015.

[6] D. Amitrano, G. Di Martino, A. Iodice, D. Riccio, and G. Ruello, "Unsupervised rapid flood mapping using Sentinel-1 GRD SAR images," *IEEE Trans. Geosci. Remote Sens.*, vol. 56, no. 6, pp. 3290–3299, Jun. 2018.

[7] Y. Li, C. Peng, Y. Chen, L. Jiao, L. Zhou, and R. Shang, "A deep learning method for change detection in synthetic aperture radar images," *IEEE Trans. Geosci. Remote Sens.*, vol. 57, no. 8, pp. 5751–5763, Mar. 2019.

[8] M. Gong, H. Yang, and P. Zhang, "Feature learning and change feature classification based on deep learning for ternary change detection in SAR images," *J. Photogramm. Remote Sens.*, vol. 129, pp. 212–225, Jul. 2017.

[9] M. Zhao, Q. Ling, and F. Li, "An iterative feedback-based change detection algorithm for flood mapping in SAR images," *IEEE Geosci. Remote Sens. Lett.*, vol. 16, no. 2, pp. 231–235, Feb. 2019.

[10] L. Bruzzone and D. F. Prieto, "An adaptive semiparametric and context-based approach to unsupervised change detection in multitemporal remote-sensing images," *IEEE Trans. Image Process.*, vol. 11, no. 4, pp. 452–466, Apr. 2002.

[11] H. Zhuang, Z. Tan, K. Deng, and H. Fan, "It is a misunderstanding that log ratio outperforms ratio in change detection of SAR images," *Eur. J. Remote Sens.*, vol. 52, no. 1, pp. 484–492, Aug. 2019.

[12] Y. Bazi, L. Bruzzone, and F. Melgani, "An unsupervised approach based on the generalized Gaussian model to automatic change detection in multitemporal SAR images," *IEEE Trans. Geosci. Remote Sens.*, vol. 43, no. 4, pp. 874–887, Apr. 2005.

[13] E. J. M. Rignot and J. J. van Zyl, "Change detection techniques for ERS-1 SAR data," *IEEE Trans. Geosci. Remote Sens.*, vol. 31, no. 4, pp. 896–906, Jul. 1993.

[14] J. Inglada and G. Mercier, "A new statistical similarity measure for change detection in multitemporal SAR images and its extension to multiscale change analysis," *IEEE Trans. Geosci. Remote Sens.*, vol. 45, no. 5, pp. 1432–1445, May 2007.

[15] S. Parrilli, M. Poderico, C. V. Angelino, and L. Verdoliva, "A nonlocal SAR image denoising algorithm based on LLMMSE wavelet shrinkage," *IEEE Trans. Geosci. Remote Sens.*, vol. 50, no. 2, pp. 606–616, Feb. 2012.

[16] L. Su, M. Gong, and B. Sun, "Change detection in synthetic aperture radar images based on non-local means with ratio similarity measurement," *Int. J. Remote Sens.*, vol. 35, no. 22, pp. 7673–7690, Nov. 2014.

[17] M. Gong, Y. Cao, and Q. Wu, "A neighborhood-based ratio approach for change detection in SAR images," *IEEE Geosci. Remote Sens. Lett.*, vol. 9, no. 2, pp. 307–311, Mar. 2012.

[18] Y. Zheng, X. Zhang, B. Hou, and G. Liu, "Using combined difference image and k-means clustering for SAR image change detection," *IEEE Geosci. Remote Sens. Lett.*, vol. 11, no. 3, pp. 691–695. Mar. 2013.

[19] L. Jia, M. Li, Y. Wu, P. Zhang, G. Liu, H. Chen, and L. An, "SAR image change detection based on iterative label-information composite kernel supervised by anisotropic texture," *IEEE Trans. Geosci. Remote Sens.*, vol. 53, no. 7, pp. 3960–3973, Jul. 2015.

[20] H. Zhuang, K. Deng, H. Fan, and S. Ma, "A novel approach based on structural information for change detection in SAR images," *Int. J. Remote Sens.*, vol. 39, no. 8, pp. 2341–2365, Jan. 2018.

[21] M. N. Sumaiya and R. S. S. Kumari, "Logarithmic mean-based thresholding for SAR image change detection," *IEEE Geosci. Remote Sens. Lett.*, vol. 13, no. 11, pp. 1726–1728, Nov. 2016.

[22] N. R. Pal and J. C. Bezdek, "On cluster validity for the fuzzy c-means model," *IEEE Trans. Fuzzy Syst.*, vol. 3, no. 3, pp. 370–379, Aug. 1995.

[23] S. Krinidis and V. Chatzis, "A robust fuzzy local information C-means clustering algorithm," *IEEE Trans. Image Process.*, vol. 19, no. 5, pp. 1328–1337, May 2010.

[24] R. Shang, L. Qi, L. Jiao, R. Stolkin, and Y. Li, "Change detection in SAR images by artificial immune multi-objective clustering," *Eng. Appl. Artif. Intell.*, vol. 31, pp. 53–67, May 2014.

[25] R. Shang, Y. Yuan, L. Jiao, Y. Meng, and A. M. Ghalamzan, "A self-paced learning algorithm for change detection in synthetic aperture radar images," *Signal Process.*, vol. 142, pp. 375–387, Jan. 2018.

[26] F. Gao, J. Dong, B. Li, and Q. Xu, "Automatic change detection in synthetic aperture radar images based on PCANet," *IEEE Geosci. Remote Sens. Lett.*, vol. 13, no. 12, pp. 1792–1796, Dec. 2016.

[27] O. Yousif and Y. Ban, "Improving SAR-based urban change detection by combining MAP-MRF classifier and nonlocal means similarity weights," *IEEE J. Sel. Topics Appl. Earth Observ. Remote Sens.*, vol. 7, no. 10, pp. 4288–4300, Oct. 2014.

[28] L. Jia, T. Zhang, J. Fang, and F. Dong, "Multiple kernel graph cut for SAR image change detection," *Remote Sens.*, vol. 13, no. 4, p. 725, Feb. 2021.

[29] J. Wang, X. Yang, L. Jia, X. Yang, and Z. Dong, "Pointwise SAR image change detection using stereo-graph cuts with spatio-temporal information," *Remote Sens. Lett.*, vol. 10, no. 5, pp. 421–429, Feb. 2019.

[30] R. Xu, Y. Xu, and Y. Quan, "Structure-texture image decomposition using discriminative patch recurrence," *IEEE Trans. Image Process.*, vol. 30, pp. 1542–1555, 2021.

[31] S. Gu, D. Meng, W. Zuo, and L. Zhang, "Joint convolutional analysis and synthesis sparse representation for single image layer separation," in *Proc. IEEE ICCV*, Venice, Italy, Oct. 2017, pp. 22–29.

[32] L. Xu, Q. Yan, Y. Xia, and J. Jia, "Structure extraction from texture via relative total variation," *ACM Trans. Graph.*, vol. 31, no. 6, pp. 1–10, Nov. 2012.

[33] P. Theologou, I. Pratikakis, and T. Theoharis, "Unsupervised spectral mesh segmentation driven by heterogeneous graphs," *IEEE Trans. Pattern Anal. Mach. Intell.*, vol. 39, no. 2, pp. 397–410, Feb. 2017.

[34] J. Wang, X. Yang, X. Yang, L. Jia, and S. Fang, "Unsupervised change detection between SAR images based on hypergraphs," *ISPRS J. Photogramm. Remote Sens.*, vol. 164, pp. 61–72, Jun. 2020.

[35] C.-A. Deledalle, L. Denis, and F. Tupin, "Iterative weighted maximum likelihood denoising with probabilistic patch-based weights," *IEEE Trans. Image Process.*, vol. 18, no. 12, pp. 2661–2672, Dec. 2009.

[36] Y. Boykov and V. Kolmogorov, "An experimental comparison of min-cut/max-flow algorithms for energy minimization in vision," *IEEE Trans. Pattern Anal. Mach. Intell.*, vol. 26, no. 9, pp. 1124–1137, Sep. 2004.

[37] T. Zhang, A. Wiesel, and M. S. Greco, "Multivariate generalized Gaussian distribution: Convexity and graphical models," *IEEE Trans. Signal Process.*, vol. 61, no. 16, pp. 4141–4148, Aug. 2013.

[38] T. K. Moon, "The expectation-maximization algorithm," *IEEE Signal Process. Mag.*, vol. 13, no. 6, pp. 47–60, Nov. 1996.

[39] M. Gong, Z. Zhou, and J. Ma, "Change detection in synthetic aperture radar images based on image fusion and fuzzy clustering," *IEEE Trans. Image Process.*, vol. 21, no. 4, pp. 2141–2151, Apr. 2012.

[40] J. Kittler and J. Illingworth, "Minimum error thresholding," *Pattern Recognit.*, vol. 19, no. 1, pp. 41–47, 1986.

[41] T. Celik, "Unsupervised change detection in satellite images using principal component analysis and k-means clustering," *IEEE Geosci. Remote Sens. Lett.*, vol. 6, no. 4, pp. 772–776, Oct. 2009.

[42] M. Gong, Y. Li, L. Jiao, M. Jia, and L. Su, "SAR change detection based on intensity and texture changes," *ISPRS J. Photogramm. Remote Sens.*, vol. 93, pp. 123–135, Jul. 2014.

[43] R. Shang, K. Xie, M. A. Okoth, and L. Jiao, "SAR image change detection based on mean shift pre-classification and fuzzy C-Means," in *Proc. IGARSS*, Yokohama, Japan, Jul. 2019, pp. 2358–2361.

[44] M. Gong, L. Su, M. Jia, and W. Chen, "Fuzzy clustering with a modified MRF energy function for change detection in synthetic aperture radar images," *IEEE Trans. Fuzzy Syst.*, vol. 22, no. 1, pp. 98–109, Feb. 2014.

[45] J. Kerekes, "Receiver operating characteristic curve confidence intervals and regions," *IEEE Geosci. Remote Sens. Lett.*, vol. 5, no. 2, pp. 251–255, Apr. 2008.

JUN WANG received the M.S. degree in computer technology from the Anhui University of Technology, China, in 2013, and the Ph.D. degree in signal and information processing from the Hefei University of Technology, China, in 2020. He is currently a Lecturer with the School of Mechanical Engineering, Quzhou University. His current research interests include computer vision, image interpretation, and change detection.

ANJUN ZHANG received the M.S. degree in information and communication engineering and the Ph.D. degree in signal and information processing from the Hefei University of Technology, China, in 2012 and 2020, respectively. He is currently a Lecturer with the School of Internet, Anhui University. His current research interests include computer vision, deep learning, and SAR image classification.